

The Influence of Mo Content and Annealing on the Oxidation Behavior of Arc-Melted Cr–xMo–8Si Alloys

Lisa Koliotassis,* Emma M. H. White, and Mathias C. Galetz

The influence of Mo (10–40 at%) additions to Cr–8 at%Si is systematically studied by analyzing arc-melted alloys in the as-cast and annealed state. The oxidation resistance is tested by thermogravimetric analysis (TGA) at 1200 °C in air for up to 100 h. Samples are characterized by X-ray diffraction, scanning electron microscopy, and wavelength-dispersive X-ray spectroscopy. The studied Cr–xMo–8Si alloy series shows a beneficial effect of Mo on the corrosion behavior. For all of the investigated Mo contents, no nitridation is observed and the oxide scale adhesion is improved. An increased amount of intermetallic A15 phase leads to the formation of a SiO₂ scale beneath the Cr₂O₃ layer during high-temperature exposure. The internal SiO₂ layer inhibits further internal oxidation of the A15 phase. Uniform size and distribution of A15, benefits the formation of a duplex oxide scale. Cr–25Mo–8 at%Si, shows the most promising oxidation behavior. The TGA data follows the parabolic law, with both the growth rate, k_p , and volatilization rate, k_v , of Cr₂O₃ being reduced by adding 10–25 at% Mo. A binary Cr/Mo–Si phase diagram is generated in order to determine accurate annealing conditions and estimate the stability range of the metastable σ phase.

1. Introduction

One possibility to decrease efficiency losses in high-temperature applications, such as gas turbines, is to exchange the state-of-the-art Ni-based superalloys with materials that do not require additional internal cooling.^[1,2] This can be realized by materials that allow higher service temperatures while retaining high mechanical strength, such as refractory metal alloys.^[1,3] One promising base material candidate among the refractory metals is chromium.^[4] Cr as a base material has a lower density and higher melting temperature when compared to nickel, while being abundant and reasonably priced.^[5–7] Challenges in developing Cr-based alloys are mainly connected to high-temperature

mechanisms like fast nitridation, as well as the spallation and evaporation of protective chromia layers above 1000 °C^[8–10] An often-discussed additional challenge is the high ductile-to-brittle transition temperature (DBTT) of Cr, which has been linked to impurities and can be influenced by alloying.^[1,4,11,12]

Alloying Cr with 4–15 at% Si leads to the formation of a two-phase microstructure composed of an A2 (Cr_{ss}) matrix and nitridation-resistant A15 (Cr₃Si) precipitates,^[13,14] resulting in increased mechanical strength at high temperatures,^[15,16] higher oxidation resistance,^[14] decreased nitridation of A2, and lower volatilization of chromia at 1200 °C.^[14,17] With more Si added to Cr, the A15 phase fraction increases and thus the oxidation properties improve. On the downside, additional Si lowers the fracture toughness at low temperatures,^[15,18] which limits application as structural material.

Alloying Mo as a ternary element results in the substitution of Cr by Mo in both the A2 and A15 phases.^[19] Matrix coarsening resistance, solid solution hardening of A2, further improvement of creep properties of the A15 phase, and promoted SiO₂ formation have all been attributed to Mo alloying.^[16,20] Adding up to 2 at% Mo resulted in an equal distribution of Mo between the A2 and A15 phases and reduced nitridation of the solid solution while further decreasing the volatilization rate during exposure in air at 1200 °C.^[20] Recent studies showed that adding approximately 32 at% Mo to Cr–13.5 at%Si fully suppressed nitridation.^[21] Stability of the system in the Mo pesting regime of 800 °C has also been confirmed.^[21] The ternary Cr–Mo–Si system is well described in the literature.^[22–24] Rudy et al. state that the Cr–Mo–Si system contains a metastable σ phase (Cr_{0.39-0.57}Mo_{0.29-0.47}Si₁₄).^[25] The stability regime of the σ phase is under discussion,^[22] which is important because the formation of the σ phase can produce cracks during processing and it is transformed into A2 and A15 when annealed at 1200 °C.^[25]

This work systematically investigates the microstructure development, phase formation, and high-temperature oxidation resistance of arc-melted Cr-rich Cr–xMo–8Si alloys ($x = 10–40$ at%) as a function of the Mo content and annealing temperatures. The Si content was fixed at 8 at% in order to prevent initial A15 phase formation in the as-cast (AC) arc-melted ingots and to allow a reasonable fracture toughness. The AC state was compared to the annealed (AN) state through determining phase

L. Koliotassis, E. M. H. White, M. C. Galetz
High Temperature Alloys
DEHEMA Research Institute
Theodor-Heuss-Allee 25, 60486 Frankfurt am Main, Germany
E-mail: lisa.koliotassis@dechema.de

 The ORCID identification number(s) for the author(s) of this article can be found under <https://doi.org/10.1002/adem.202301906>.

© 2024 The Authors. Advanced Engineering Materials published by Wiley-VCH GmbH. This is an open access article under the terms of the Creative Commons Attribution License, which permits use, distribution and reproduction in any medium, provided the original work is properly cited.

DOI: 10.1002/adem.202301906

compositions and microstructures. Thermogravimetric analysis (TGA) tests were performed in air at 1200 °C for up to 100 h to evaluate the influence of varying Mo content in Cr-*x*Mo-8Si alloys on the oxidation resistance.

2. Results and Discussion

2.1. Microstructure and Phase Analysis

2.1.1. Arc-Melted Samples

X-ray diffraction (XRD) results of the AC Cr-*x*Mo-8Si series are depicted in **Figure 1**. All samples contain the cubic A2 phase of Cr. As Mo is fully soluble in the A2 Cr phase and is the larger atom,^[19,26] increasing the Mo content leads to a shift in the A2 reflections to lower angles, corresponding to a larger LP. No primary precipitation of intermetallic (Cr,Mo)₃Si phase (A15) phase was observed in the Cr-8Si reference sample. For the 10 and 20 at% Mo samples, a slight indication for A15 phase was visible, whereas the samples with 25 and 40 at% Mo show the formation of σ phase instead.

These results are confirmed by WDS measurements (**Table 1**). For 20, 25, and 40 at% Mo, two A2 phases were observed: “A2_B” is richer in Mo and poorer in Si than the “A2_A.” This segregation within the A2 explains the increasing broadening of the XRD reflection of the Cr solid solution.

EPMA maps of the Cr-*x*Mo-8Si series (**Figure 2**) show the semiquantitative distribution of elements in the microstructure. Note that the A15 phase is not present in these images due to the very minor amount present in only the 10 and 20 at% Mo samples. An increased Mo content in the Cr-*x*Mo-8Si system leads to increasing inhomogeneity in the elemental distribution. For 10 at% Mo, the distribution of all elements appears homogeneous, while the 20–40 at% Mo samples show increasing segregation, as reflected in the broadening of the A2 reflection (**Figure 1**) and the two types of A2 reported in **Table 1**. Strong dendritic solidification is observed for Mo contents of 25 and 40 at%, where the σ phase is present. Mo is preferably enriched in Si-poor areas, which is the location of A2 phase.

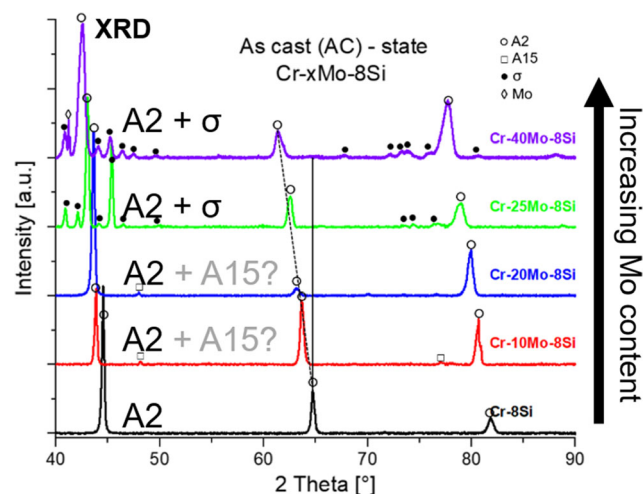


Figure 1. XRD of AC states of the Cr-*x*Mo-8Si alloy series.

Table 1. EPMA/WDS quantitative measurements of the observed phases in the AC states.

Nominal composition	Phase	Cr [at%]	Mo [at%]	Si [at%]
Cr-10Mo-8Si	A2	82.9	1.4	10.0
	A15	70.0	0.2	11.2
Cr-20Mo-8Si	A2_A	74.5	0.4	18.2
	A2_B	74.8	0.3	19.0
	A15	65.4	0.2	17.4
Cr-25Mo-8Si	A2_A	68.1	1.0	25.1
	A2_B	66.2	1.0	28.6
	σ	64.1	0.8	23.0
Cr-40Mo-8Si	A2_A	52.6	3.1	42.1
	A2_B	45.0	1.6	51.6
	σ	56.7	2.0	31.0

2.1.2. Annealed States

The two types of anneals that were performed were under the same Ar/5%H₂ atmosphere for the same duration of 100 h and were both followed by a water quench (Q); thus, the only difference was the temperature of 1200 °C or 1350 °C. **Figure 3** shows the diffractograms and calculated LPs for the 1200 and 1350 °C anneals of the Cr-*x*Mo-8Si series. After annealing at 1200 °C for 100 h, all samples of the Cr-*x*Mo-8Si series showed formation of the A15 phase in addition to the A2 solid solution. The formerly visible σ phase decomposed to A15 and A2 in both cases, which is in line with the suggested phase diagram presented in ref. [22]. For the anneal at 1350 °C, the behavior is similar except for the sample containing 40 at% Mo. For 40 at% Mo, some A15 did form but the σ phase remained, suggesting the stable regime of the σ phase is in line with the ternary diagram for Cr-Si-Mo at 1300 °C in ref. [22].

The calculated LPs of the A15 and A2 phases are plotted against the Cr/Mo ratio (as determined by WDS) in **Figure 3c**. The LP of the A2 phase ranges from a minimum 2.92 Å (Cr-*x*Mo-8Si with *x* = 10 at%) to a maximum of 3.02 Å (Cr-*x*Mo-8Si with *x* = 40 at%), whereas the LP for the A15 phase varies between 4.62 and 4.72 Å. Interestingly, in both cases an increase of about 0.1 Å results for the same overall increase in Mo content (Cr-*x*Mo-8Si with 10 vs 40 at% Mo), even though the Mo contents in the respective phases are not the same (higher in A2 than in A15, see Section 2.1.3). After both anneals, the LPs of the A2 phases are consistent with the literature data.^[19,27]

Microstructural observations (see Section 2.1.3) of both anneals (1200 and 1350 °C) show that for the lower 1200 °C anneal and the samples with Mo contents ≥ 25 at%, the strongly pronounced dendritic microstructure from the AC condition determines the regions where the A15 phase formed (predominantly in the formerly Si-rich areas). The overall distribution of the A15 phase is thus inhomogeneous. For Mo contents ≤ 20 at%, A15 precipitation along the grain boundaries is dominant. The A15 precipitates inside the grains are also rather irregularly spread. For the higher 1350 °C anneal, the A15 precipitates coarsened and were overall fewer in quantity, but were

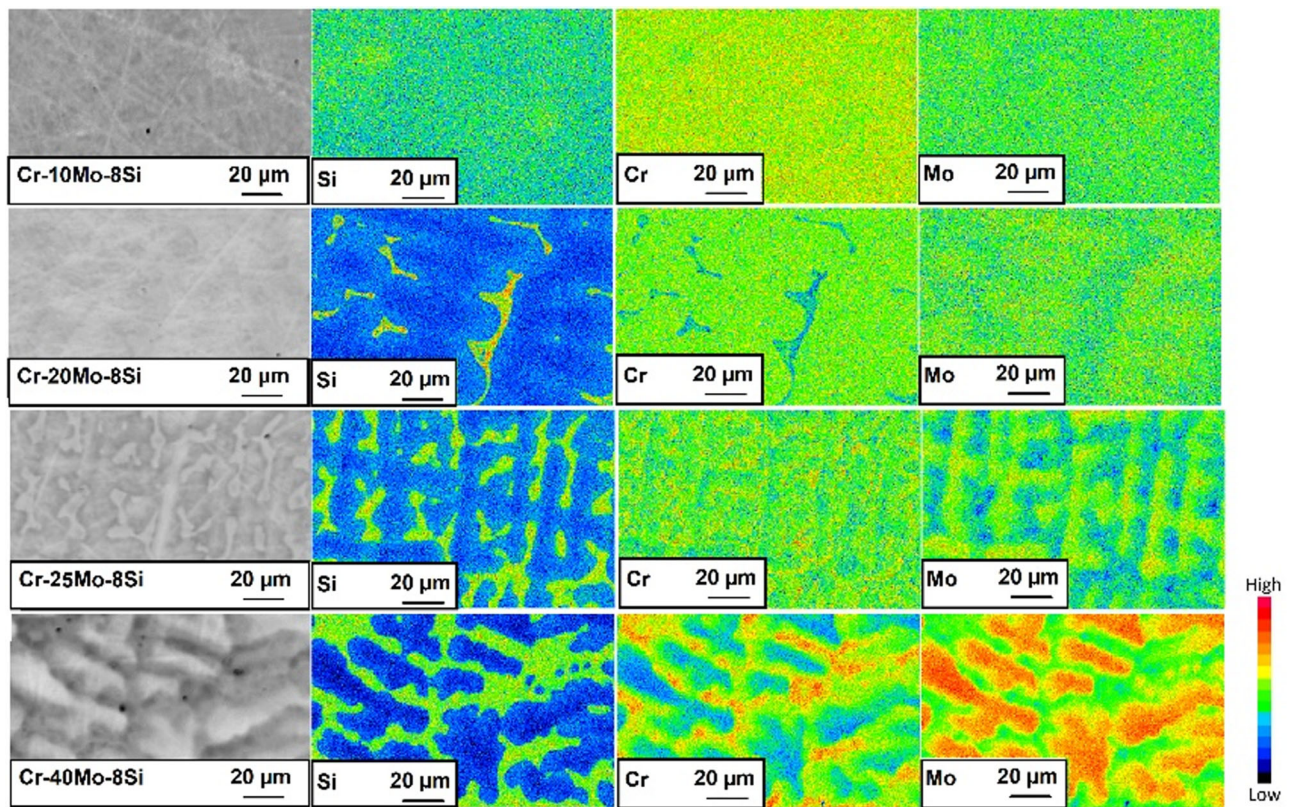


Figure 2. EPMA/WDS maps of AC states of the Cr-xMo-8Si alloy series.

more homogeneous in size and distribution, especially for Cr-25Mo-8Si. Grain boundary precipitation of the A15 phase was observed for 10 and 20 at% Mo after the 1200 °C anneal, while this effect was only dominant for the 10 at% Mo sample after the 1350 °C anneal. An increased Mo content appears to reduce the grain boundary precipitation of A15. Similar effects have been described in refs. [16,28] for low Mo contents of 2 at%. Higher temperature annealing provides the additional benefit of reducing grain boundary precipitates.

Using phase compositional data from wavelength-dispersive X-ray spectroscopy (EPMA/WDS), the influence of the Mo content on the Mo distribution inside the phases, the Si solubility, and the overall amount of A15 phase was analyzed (Figure 4a-c). The distribution coefficient, k , was calculated via Equation (1):

$$k = \frac{c_{\text{Mo}}(\text{A15})}{c_{\text{Mo}}(\text{A2})} \quad (1)$$

It can be seen even though Mo is present in both phases (A2 and A15), Mo is preferably enriched in the A2 phase and this effect increases with increasing Mo content and is stronger for the lower 1200 °C anneal (Figure 4a). The Si solubility decreases linearly in both phases with increasing Mo content (Figure 4b). This leads to an increasing amount of intermetallic A15 phase with increasing Mo content (Figure 4c). One extra sample containing 35 at% Mo was produced and added to the 1200 °C anneal to confirm that a plateau is approached at around 35 area percent of A15 due to the limited overall Si content (8 at%).

The proportion of the A15 phase is strongly reduced in Cr-40Mo-8Si due to the presence of the σ phase.

2.1.3. Quasibinary Cr/Mo – Si Phase Diagram

To gain a better understanding of annealing conditions for arc-melted Cr-xMo-8Si samples, the WDS data (Table 2) were used to develop a quasibinary Cr/Mo-Si phase diagram (Figure 5). For this purpose, a third annealing at 1450 °C was performed and Si solubilities of A2 and A15 phases were added and compared to the literature data for the Cr-Si and Mo-Si binary phase diagrams.

A stable regime of the σ phase was observed for 25 and 40 at% Mo at 1450 and 1350 °C, respectively. Increasing the Mo content in Cr-xMo-8Si shifts the phase boundary between the A2 single-phase field and the A2 + A15 regime, as well as between the A15 + A2 and A15 single-phase field, to lower Si contents when compared to the Cr-Si system.

To further improve the distribution of the intermetallic A15 phase inside the solid solution A2 matrix, a two-step precipitation hardening anneal would likely be beneficial. This type of anneal consists of a homogenization step at high temperature, entering the single-phase field (A2) and adding a precipitation anneal at a lower temperature (two-phase field of A2 + A15). For the studied alloy series, temperatures of >1600 °C would be necessary to enter the single-phase field, which can result in rather strong Cr evaporation during the anneal. Also due to uncertainty about

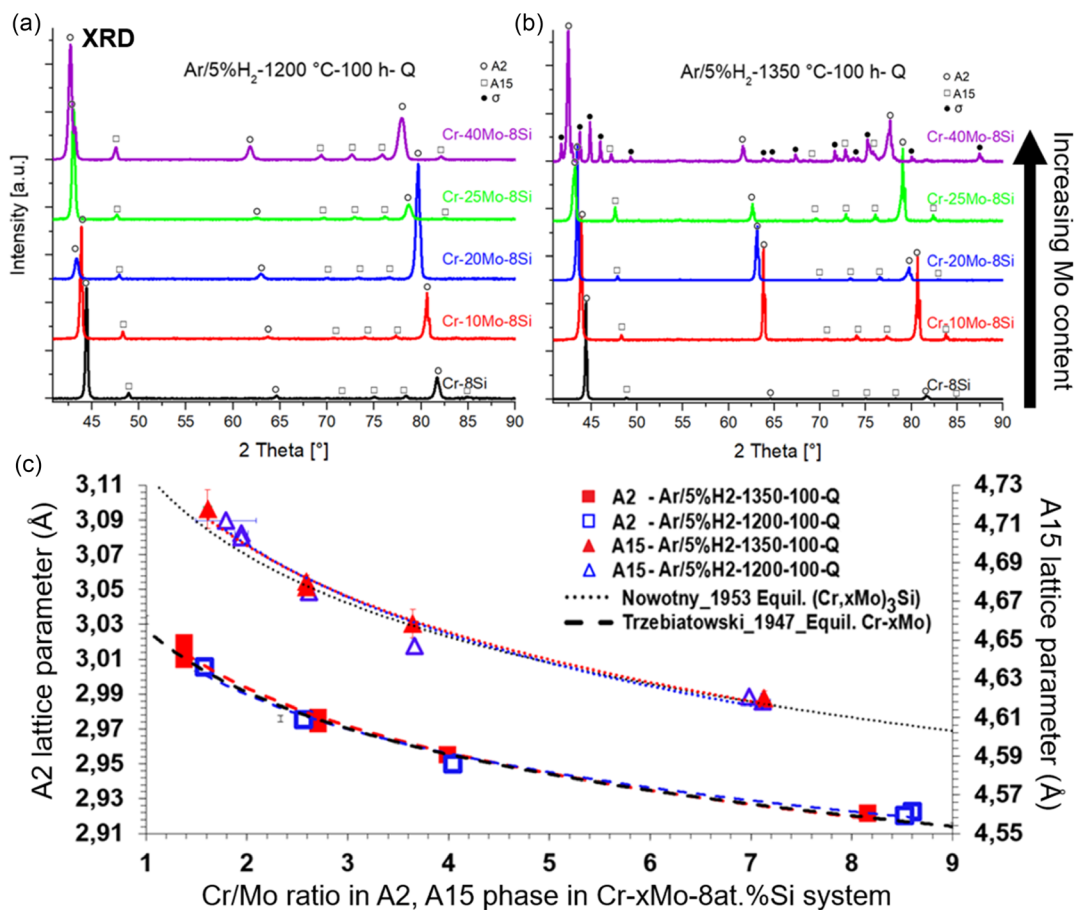


Figure 3. a) XRD after 1200 °C anneal; b) XRD after 1350 °C anneal; and c) LPs of A2 and A15 phases as a function of the Cr/Mo ratio including the trendlines for the literature data of refs. [19,27].

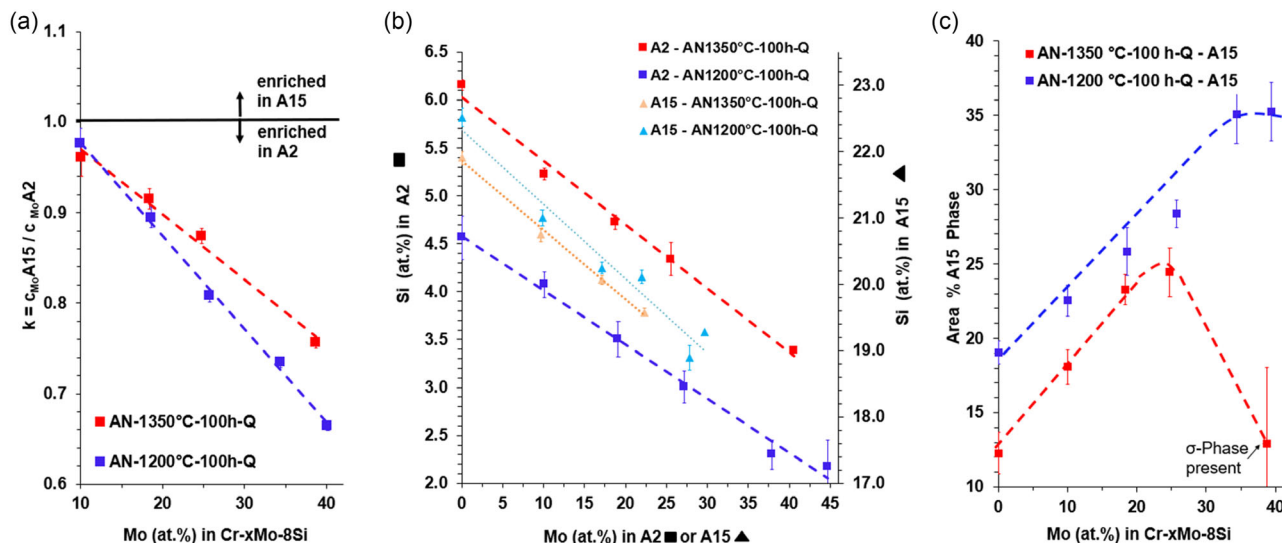


Figure 4. Influence of Mo content on the a) Mo distribution, b) Si solubility, and c) amount of A15 phase.

Table 2. WDS analysis of investigated samples.

Nominal	Phase	Ar/5%H ₂ -1200 °C-100 h-Q									
		Cr [at%]		Mo [at%]		Si [at%]		Cr/Mo		Area [%]	
Cr-8Si	All	92.0	0.1	-	-	8.0	0.1	-	-	100	
	A2	95.4	0.2	-	-	4.6	0.2	-	-	81.0	2.0
	A15	77.5	0.1	-	-	22.5	0.1	-	-	19.0	0.8
Cr-10Mo-8Si	All	82.1	0.1	10.0	0.1	7.9	0.1	8.20	0.01	100	
	A2	85.9	0.1	10.1	0.1	4.1	0.1	8.53	0.01	77.5	2.0
	A15	69.2	0.1	9.8	0.1	21.0	0.1	7.03	0.01	22.5	1.1
Cr-20Mo-8Si	All	73.6	0.1	18.6	0.1	7.8	0.1	3.95	0.01	100	
	A2	77.4	0.1	19.1	0.1	3.5	0.2	4.05	0.01	74.2	2.0
	A15	62.7	0.1	17.1	0.1	20.2	0.1	3.66	0.01	25.8	1.6
Cr-25Mo-8Si	All	66.4	0.1	25.7	0.1	7.9	0.1	2.58	0.00	100	
	A2	69.8	0.1	27.2	0.1	3.0	0.2	2.57	0.01	71.6	2.0
	A15	57.9	0.1	22.0	0.1	20.1	0.1	2.64	0.01	28.4	0.9
Cr-40Mo-8Si	All	52.4	0.1	39.4	0.1	8.2	0.2	1.33	0.00	100	
	A2	53.1	0.1	44.7	0.1	2.2	0.3	1.19	0.01	64.8	2.0
	A15	51.0	0.1	29.7	0.1	19.3	0.2	1.72	0.01	35.2	2.0
Nominal	Phase	Ar/5%H ₂ -1350 °C-100 h-Q									
		Cr [at%]		Mo [at%]		Si [at%]		Cr/Mo		Area [%]	
Cr-8Si	All	91.9	0.1	-	-	8.1	0.1	-	-	100	
	A2	93.8	0.1	-	-	6.2	0.1	-	-	87.7	2.0
	A15	78.1	0.1	-	-	21.9	0.1	-	-	12.3	1.4
Cr-10Mo-8Si	All	81.9	0.1	10.0	0.1	8.0	0.1	8.17	0.01	100	
	A2	84.7	0.1	10.1	0.1	5.2	0.1	8.38	0.01	81.9	2.0
	A15	69.5	0.1	9.7	0.1	20.7	0.1	7.16	0.01	18.1	1.2
Cr-20Mo-8Si	All	73.3	0.1	18.4	0.1	8.3	0.1	3.99	0.01	100	
	A2	76.5	0.1	18.7	0.1	4.7	0.1	4.08	0.01	76.7	2.0
	A15	62.8	0.1	17.1	0.1	20.1	0.1	3.66	0.01	23.3	1.0
Cr-25Mo-8Si	All	67.2	0.1	24.8	0.1	8.1	0.1	2.71	0.01	100	
	A2	70.1	0.1	25.5	0.1	4.3	0.2	2.74	0.01	75.6	2.0
	A15	58.1	0.1	22.3	0.1	19.6	0.1	2.60	0.01	24.4	1.6
Cr-40Mo-8Si	All	53.1	0.7	38.3	0.7	8.6	0.7	1.38	0.03	100	
	A2	56.0	0.1	40.6	0.1	3.4	0.1	1.38	0.01	53.5	4.0
	A15	48.7	0.1	30.7	0.1	20.6	0.1	1.59	0.01	12.9	6.0
	σ	50.0	0.8	37.6	0.8	12.4	0.5	1.33	0.04	33.6	4.0
Nominal	Phase	Ar/5%H ₂ -1450 °C-20 h-Q									
		Cr [at%]		Mo [at%]		Si [at%]		Cr/Mo		Area [%]	
Cr-10Mo-8Si	All	81.9	0.1	10.0	0.1	8.1	0.1	8.18	0.01	100	
	A2	83.3	0.2	10.1	0.1	6.6	0.2	8.28	0.01	89.6	2.0
	A15	69.8	0.1	9.6	0.1	20.6	0.2	7.31	0.01	10.4	1.0
Cr-20Mo-8Si	All	72.2	0.0	19.8	0.1	7.9	0.1	3.64	0.01	100	
	A2	74.0	0.1	20.1	0.1	5.9	0.2	3.69	0.01	85.9	2.0
	A15	61.5	0.2	18.5	0.1	20.0	0.3	3.33	0.01	14.1	1.5
Cr-25Mo-8Si	All	61.7	0.1	30.0	0.2	8.3	0.3	2.05	0.01	100	
	A2	65.4	0.2	29.3	0.1	5.3	0.1	2.23	0.01	61.1	2.0
	A15	54.9	0.2	25.4	0.3	19.7	0.7	2.16	0.02	2.5	4.0

Table 2. Continued.

Nominal	Phase	Ar/5%H ₂ -1450 °C-20 h-Q									
		Cr [at%]		Mo [at%]		Si [at%]		Cr/Mo		Area [%]	
Cr-40Mo-8Si	σ	55.8	0.1	31.7	0.1	12.5	0.1	1.76	0.00	36.4	2.0
	All	54.5	0.0	38.1	0.1	8.4	0.1	1.43	0.00	100	
	A2	56.8	0.1	38.8	0.2	4.3	0.3	1.46	0.01	49.8	2.0
	σ	51.1	0.1	36.7	0.2	12.2	0.3	1.39	0.01	51.2	2.0

where σ phase is stable, a higher temperature anneal might lead to an A2 + σ phase mixture instead of single-phase A2. An alternative way to address even A15 distribution without heat treatment >1600 °C could be the development of a powder metallurgical production route for these kinds of alloys.

2.2. High-Temperature Corrosion Behavior in Air

2.2.1. Adhesion of Oxide Layer Versus Composition

The results of oxidation exposures of samples annealed at 1350 °C are visible in **Figure 6**. The macroimages of the alloy series exposed at 1200 °C in static laboratory air for 50 h are compared with a second experiment of cuboids exposed at 1200 °C in flowing dry synthetic air for 100 h.

Note that the difference in shape and size of the cuboids (especially the bottom row of **Figure 6**) is due to manufacturing and not due to oxidation effects. For the 50 h exposure, the reference sample without Mo is the only sample showing severe spallation of the dark gray oxide that formed. All Mo-containing samples showed no obvious spallation except for some regions near the edges of the cuboids. XRD identified the dark gray oxide as Cr₂O₃.

For the 100 h exposures in flowing air, not only the reference, but also the 10 and 20 at% Mo compositions show some spallation of the oxide, while the 25 and 40 at% Mo alloys do not show any spallation. As the cuboids with 10 and 20 at% Mo did not show sudden mass decrease during the exposure duration, it is likely that the rather harsh cooling conditions in flowing air lead to spallation.

These results suggest that Mo has a positive influence on the adhesion of the formed oxide layer as the alloys containing 25 at% Mo or more did not show spallation during the experiments. Chromia scales are known to contain compressive stresses that lead to buckling and spallation, especially when grown on pure Cr.^[17,29-31] This has been linked to the formation of a duplex oxide of outward growing columnar chromia grains and inward growing equiaxed chromia grains in oxidizing atmospheres, where the new oxide forms within the scale and creates such stresses.^[32,33] It is assumed that detachment of the external and internal part of the oxide scale occurs during cooling, causing spallation.^[32] The addition of Mo alters this scale growth mechanism and leads to lower stresses in the scale, either by doping or the creation of free volume by Mo volatilization. In either case, it prevents scale spallation.

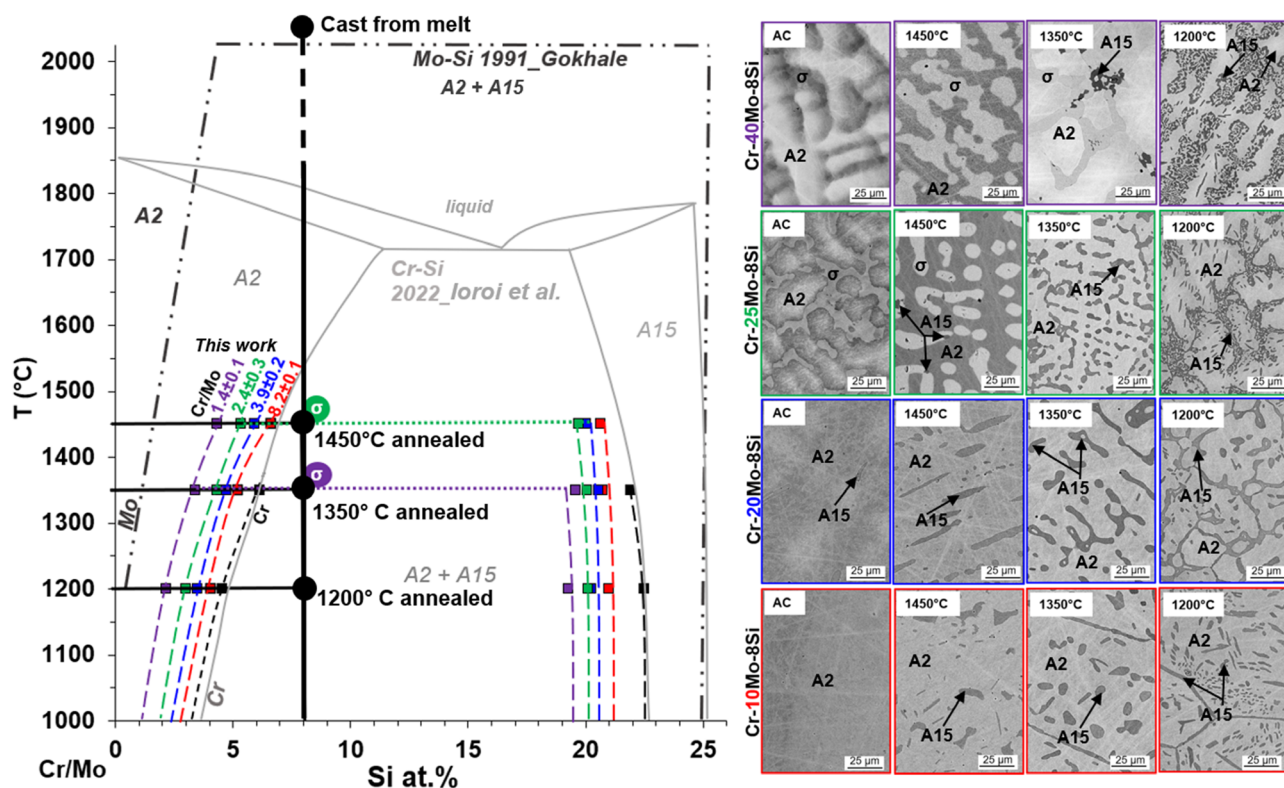


Figure 5. Graphical estimation of the quasibinary phase diagram of Cr/Mo-Si based on the studied alloys including Mo-Si and Cr-Si data from refs. [13,39] (l.); microstructures of the studied alloys after arc melting and varying anneals (r.).

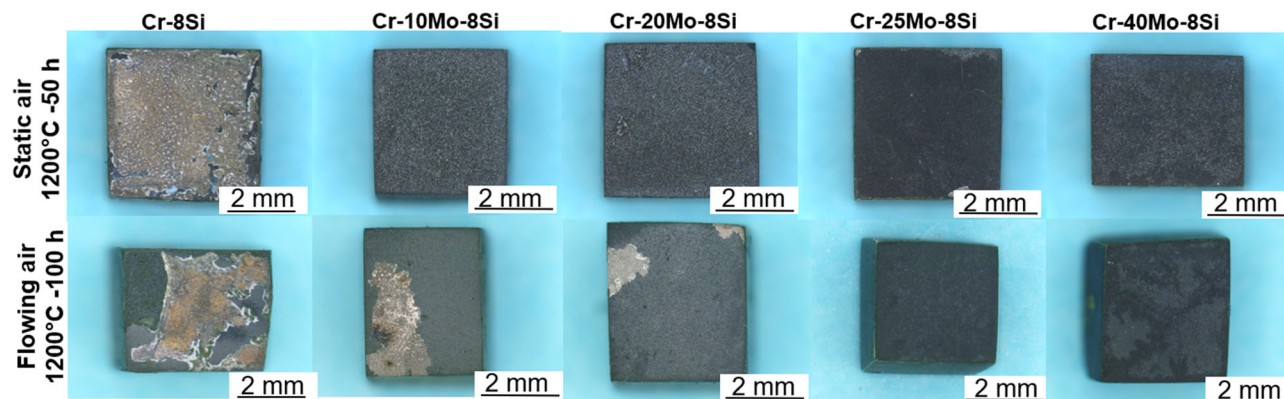


Figure 6. Cuboids after exposure at 1200°C in static and flowing air for 50 and 100 h.

2.2.2. Cross Sections—Exposure in Static Laboratory Air at 1200°C for 50 h

Electron images and EPMA/WDS maps of surface cross sections of oxidized regions of the arc-melted cuboids annealed at 1350°C and exposed at 1200°C in static laboratory air for 50 h are depicted in Figure 7.

The elemental distributions (Figure 7) show that the Cr-8Si reference is the only sample that formed a nitrogen-rich subsurface phase. Due to spallation of chromia in most areas, XRD

could confirm that Cr₂N formed in the subsurface zone. The alloys containing Mo annealed in laboratory air for 50 h at 1200°C did not show any nitridation of the Cr solid solution as compared to Cr-8Si. Mo contents ≥10 at% in Cr-xMo-8Si fully inhibit nitridation of the A2 matrix. Apart from formation of a 10 ± 2 μm chromia layer, the elemental maps of Figure 7 show internal oxidation of the former A15 precipitates, especially for 10 and 20 at% Mo. Spot measurements from WDS suggest A15 oxidizes to SiO₂. The A15 phase does seem to be nitridation resistant, but is internally oxidized for Mo contents below 25 at%.

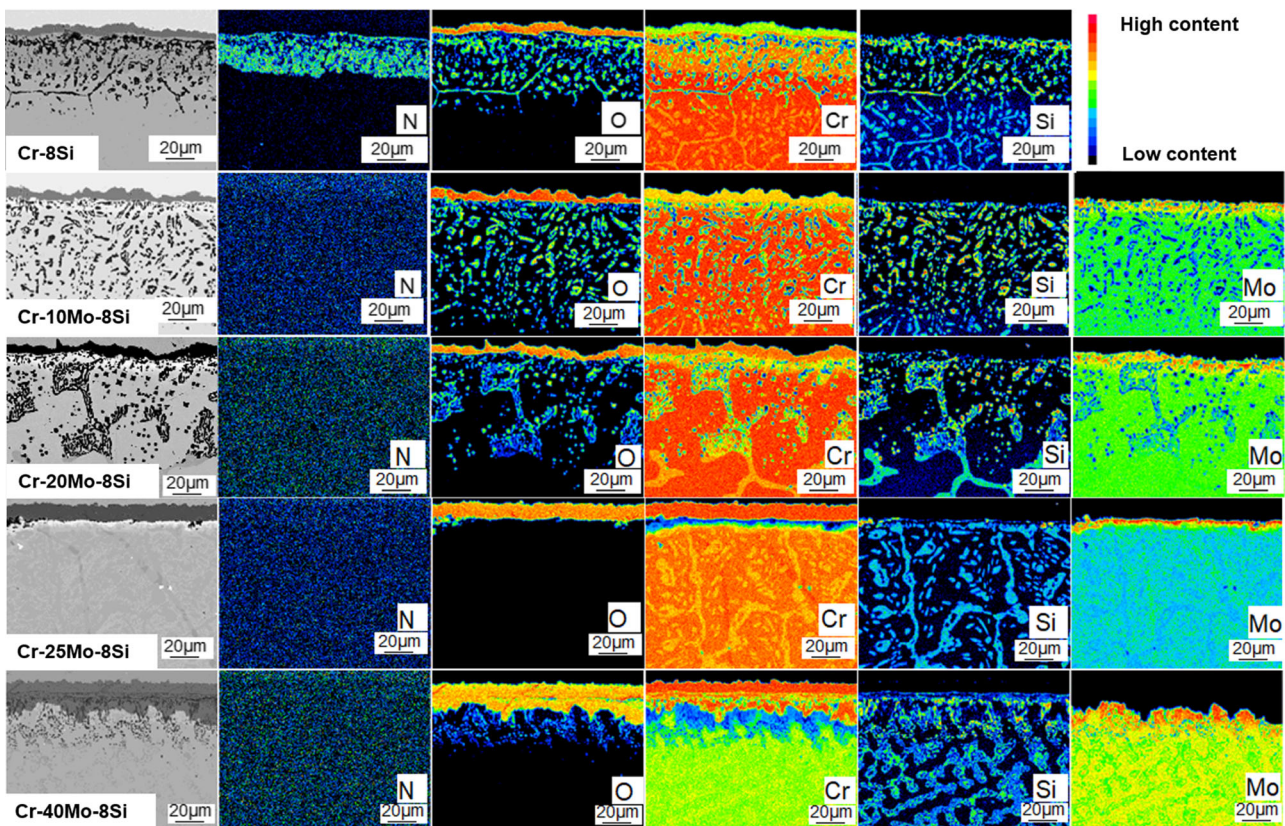


Figure 7. Surface cross-sectional electron microscope and EPMA/WDS maps of oxidized regions of varying Mo-content samples annealed at 1350 °C and exposed to static laboratory air at 1200 °C for 50 h.

For the 10 and 20 at% Mo samples, a very similar behavior is observed but the internal oxidation depth is increased and the thickness of the chromia layer is decreased as compared to the reference sample as summarized in **Table 3**. It should be noted that the images shown in Figure 7 are not the only ones

Table 3. Chromia thickness and internal oxidation depth of A15 phase in Cr-xMo-8Si after exposure at 1200 °C for 50 h in static laboratory air.

Nominal composition	Anneal T [°C]-100 h-Q	Exposure at 1200 °C in static air for 50 h	
		Chromia scale thickness d [μm]	Internal oxidation depth [μm]
Reference Cr-8Si ^{a)}	1200	10 ± 2	44 ± 9
Cr-10Mo-8Si	1200	7 ± 3	81 ± 6
	1350	6 ± 1	87 ± 6
Cr-20Mo-8Si	1200	13 ± 1	47 ± 4
	1350	6 ± 1	80 ± 2
Cr-25Mo-8Si	1200	12 ± 2	16 ± 3
	1350	11 ± 1	1 ± 4
Cr-40Mo-8Si	1200	21 ± 3	38 ± 9
	1350	23 ± 5	18 ± 1

^{a)}Nitridation of A2 and strong spallation of chromia observed.

used for determination of the average scale thicknesses and oxidation depths. The A2 phase is Si depleted in the interdiffusion zone, which is especially visible for 0 to 20 at% Mo in Figure 7. Surprisingly, Cr-25Mo-8Si shows almost no internal oxidation of the A15 phase, but a rather thick continuous chromia layer. However, 40 at% Mo shows not only outward growing chromia, but also inward growth of the oxide, separated by discontinuous SiO₂ particles that likely developed out of former A15 phase precipitates. Cr-40Mo-8Si overall shows the thickest chromia scale (23 ± 5 μm) and a rather low internal oxidation depth of A15 when compared to the reference sample without Mo.

Mo is strongly enriched in the layer beneath the oxide scale, forming a Mo-enriched A2 phase. The outer chromia oxide layer thickness increases with increasing Mo content, while the penetration depth of the internal oxidation (A15 → SiO₂) decreases simultaneously.

The exceptionally good oxidation behavior of Cr25-Mo-8Si can be explained through a closer examination of the subscale beneath the chromia layer (**Figure 8**). Negligible internal oxidation occurs, and instead a continuous SiO₂ subscale forms beneath the chromia layer. There appears to be a threshold of Mo content that increases the Si activity to a degree where Si outward diffusion is faster than O inward diffusion, and thus, initially a dense SiO₂ layer below the Cr₂O₃ layer is able to form. In addition to the increase in Si activity, however, a minimum

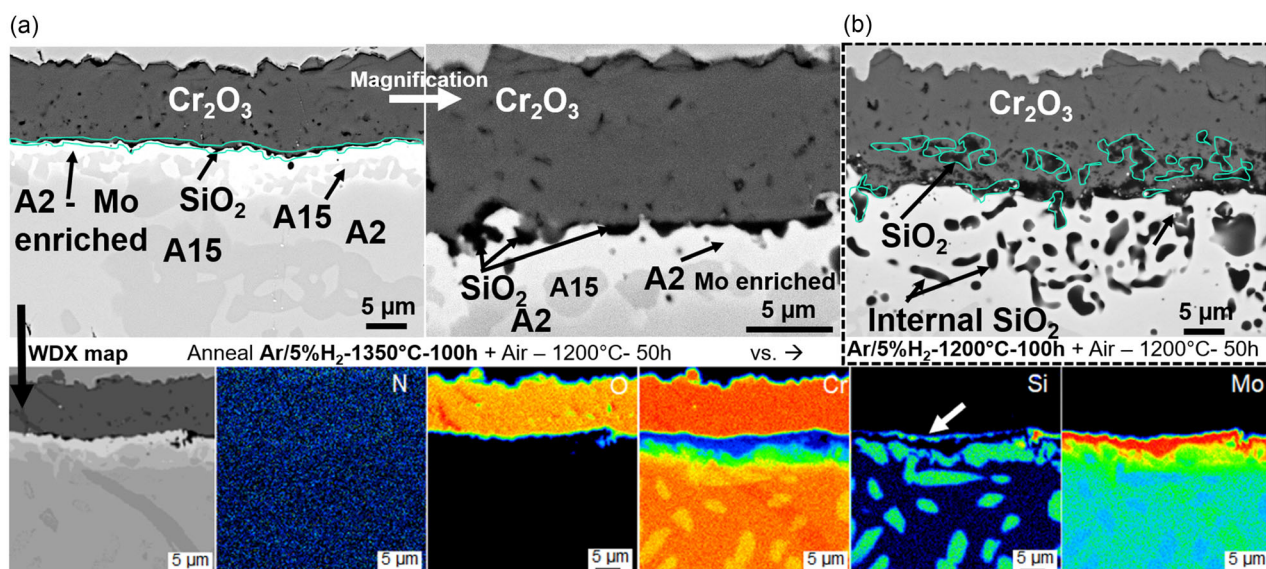


Figure 8. Scanning electron microscopy images and EPMA/WDS maps of surface cross sections of oxidized Cr-25Mo-8Si (static air, 1200 °C for 50 h) for two different anneals: a) 1350 °C and b) 1200 °C.

fraction of A15 phase must be present and the precipitates must be within a certain proximity to each other in order to create this continuous SiO₂ layer. Figure 8b shows the oxide scale formed on a Cr-25Mo-8Si sample previously annealed at 1200 °C with a less homogenous distribution of the A15 phase. During oxidation at 1200 °C in air, this leads to the formation of discontinuous SiO₂ and thus also internal oxidation of A15 occurred. So, not only the composition, but also the annealing conditions have a large influence on the oxidation behavior of Cr-25Mo-8Si.

2.2.3. Thermogravimetric Analysis (Air-1200 °C-100 h)

The mass changes during exposure at 1200 °C in dry synthetic air for 100 h are plotted in Figure 9a. The Cr-8Si reference sample suffers from breakaway oxidation, as also described in ref. [34], after around 95 h and reaches an overall mass gain of 3.4 mg cm⁻² after 100 h. The mass gain is lower for Mo-containing samples and reaches 3.1 mg cm⁻² for Cr-10Mo-8Si, 2.3 mg cm⁻² for Cr-20Mo-8Si, and only 1.5 mg cm⁻² for Cr-25Mo-8Si. All curves up to 25 at% Mo initially show a parabolic growth rate and then

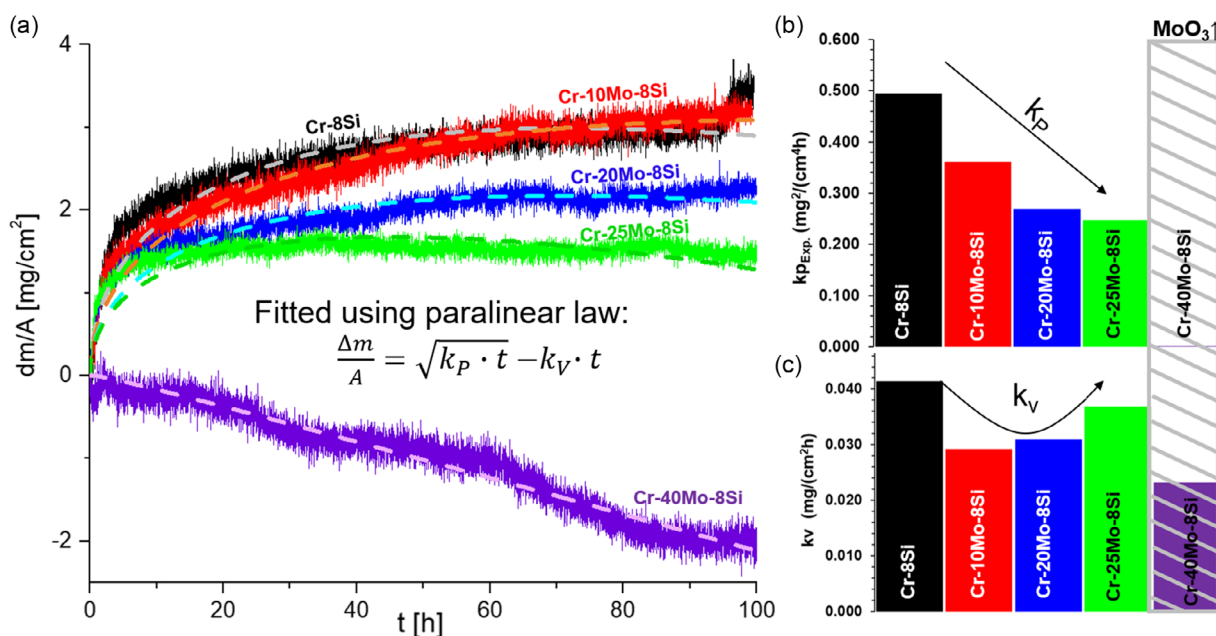


Figure 9. a) Mass changes and b) calculated parabolic (k_p) and c) volatilization rate (k_v) for exposures at 1200 °C for 100 h in flowing dry synthetic air.

change to parilinear behavior. The Cr–40Mo–8Si alloy shows continuous mass loss, reaching -2 mg cm^{-2} . The trend is not perfectly linear and hints at a rather complex process of oxide formation and volatilization of likely more than one species.

Besides some MoO_3 evaporation, the chromia scale can form the volatile oxide CrO_3 (Equation (2)) at the investigated temperature.^[10,35] Thus, the mass gain of the specimens can be described by a parabolic growth rate, k_p , and a linear volatilization rate, k_v . Therefore, the parilinear law depicted in Equation (3) was used to fit all of the mass gain curves and determine values of k_p and k_v as included in Figure 9b,c. The origin of the parilinear law used here is described in ref. [10].



$$\frac{\Delta m}{A} = \sqrt{k_p t} - k_v t \quad (3)$$

The calculations show that the parabolic growth rate of the oxides decreased with increasing Mo content (Figure 9b). While the reference Cr–8Si shows a k_p of $0.4953 \text{ mg}^2 (\text{cm}^4 \text{ h})^{-1}$, it decreases to $0.2474 \text{ mg}^2 (\text{cm}^4 \text{ h})^{-1}$ for 25 at% Mo. Correspondingly, Table 3 confirms that the chromia thicknesses decrease for specimens containing 10–20 at% Mo. For Cr–25Mo–8Si, the chromia layer has a similar thickness as the Cr–8Si reference (Table 3), but the internal oxidation of A15 was inhibited and thus an overall lower k_p value is reasonable. Trying to use the parilinear fit for the Cr–40Mo–8Si alloy does not allow for good agreement with the cross sections and a reasonable value for k_p . The cross sections showed that the chromia layer is the thickest for this composition, while the calculated k_p has the lowest value of $0.004 \text{ mg}^2 (\text{cm}^4 \text{ h})^{-1}$. As this composition is the only one showing strong continuous mass loss, it is likely that not only chromia is evaporating but also large amounts of MoO_3 are also volatilizing due to the high Mo content. Additionally, some internal oxidation is evident. So, for the Cr–40Mo–8Si composition volatilization dominates the oxidation mechanisms and the parilinear law for the description of oxide growth kinetics cannot be used.

The volatilization rate, k_v (Figure 9c), for the reference sample Cr–8Si is $0.0414 \text{ mg} (\text{cm}^2 \text{ h})^{-1}$. It decreases for the Mo-containing samples to 0.0293, 0.0309, and $0.0369 \text{ mg} (\text{cm}^2 \text{ h})^{-1}$ for 10, 20, and 25 at% Mo, respectively. These values are higher than for other non-Mo-containing chromia forming alloys like, e.g., Ni–40Cr, which are around $0.0145\text{--}0.0149 \text{ mg} (\text{cm}^2 \text{ h})^{-1}$ described in refs. [36,37].

The oxide growth kinetics and adherent oxide scales of the Cr– x Mo–8Si alloys ($x = 10, 20,$ and 25 at%) show high potential for a new class of lightweight refractory alloys for high-temperature applications. Especially worthwhile of further development is the Cr–25Mo–8Si alloy with extremely low mass gain and continuous SiO_2 subscale formation, preventing internal oxidation. Future investigations will include long-term exposures up to 1000 h to see if the Mo-enriched layer beneath the duplex oxide scale remains stable, or will lead to spontaneous failure due to formation of MoO_3 . The keys to future work within this class of alloys will be avoiding σ phase formation and ensuring uniform distribution of the A15 phase, while perhaps lowering the DBTT which was not addressed in this work.

3. Conclusions

Mo additions of up to 25 at% to Cr–8Si change the microstructure of annealed arc-melted alloys and have a beneficial effect on the oxidation behavior at 1200°C in air.

Microstructural summary: 1) Mo is present in both A2 and A15 phases but is preferably enriched in A2. This effect increases with increasing Mo content. 2) Grain boundary precipitation of A15 phase is reduced for increased Mo contents and increased annealing temperature. 3) Increasing the amount of Mo leads to decreased solubility of Si in both phases (A2 + A15) and thus leads to an increasing amount of A15 phase. 4) Higher temperature anneal (1350°C vs 1200°C) of arc-melted alloys leads to less and coarser, but overall more evenly distributed, A15 precipitates. 5) A binary Cr/Mo–Si phase diagram was developed for the alloy series including an estimation of the stability range of the metastable σ phase.

Oxidation properties at 1200°C in air: 1) For all investigated Mo contents, nitridation of the A2 solid solution was fully inhibited. 2) The oxide scale adhesion was improved by Mo addition. For Mo >25 at%, no spallation was observed. 3) Below a certain phase fraction and distribution, the A15 phase is prone to internal oxidation. 4) An increased amount of A15 can lead to the formation of a continuous SiO_2 scale beneath the Cr_2O_3 external oxide layer. The continuous internal SiO_2 layer prevents further internal oxidation of the Si in the A15 phase. 5) Evaluation of TGA data using the parilinear law suggests that the parabolic growth rate, k_p , and volatilization rate, k_v , of Cr_2O_3 are reduced by adding 10–25 at% Mo.

A predictable and stable oxidation behavior was achieved for Cr–25Mo–8Si. Nitridation of the solid solution phase and internal oxidation of the intermetallic A15 phase were inhibited during exposure up to 100 h at 1200°C in flowing synthetic air, making the Cr–25Mo–8Si composition of great interest for further study.

4. Experimental Section

Synthesis of the Alloy: Chromium (Cr > 99.95 wt%, PLANSEE), silicon (Si > 99.999 wt%, GfE), and molybdenum pieces (Mo > 99.97 wt%, PLANSEE) were used to produce a CrMoSi alloy series (Mo = 10–40 at% and Si = 8 at%) via arc melting. The overall mass of each produced ingot was 7 g (resulting in ellipsoidal buttons of ca. $15 \times 10 \times 8 \text{ mm}$). The elements were weighed with a high precision balance (Mettler Toledo XP205DR/M), with a deviation of 1 mg of the calculated mass. To compensate for Cr loss during the arc melting process, 1 wt% excess Cr was added to each composition. A mini arc melting system MAM-1 (Edmund Bühler GmbH) was used to perform the arc melting process. The ingots were produced on a water-cooled Cu crucible using a nonconsumable tungsten electrode. The melting chamber was alternately evacuated and purged with Ar 5 times before melting. Also, Zr was melted twice before melting the actual sample to get any residual oxygen in the chamber. In a first step, Cr and Mo were prealloyed and subsequently Si was added. The ingots were remelted at least 5 times and flipped each time to ensure homogeneity.

Annealing: Annealing of the arc-melted samples was performed to 1) homogenize any concentration gradients and 2) achieve uniform formation of $(\text{Cr},\text{Mo})_3\text{Si}$ precipitates inside the (Cr,Mo) -solid solution matrix. All anneals were performed in a tube furnace (Carbolite type STF 14/450) in a flowing Ar/5 vol% H_2 atmosphere using an alumina tube. The samples were placed in an alumina crucible. A second crucible was used containing

Ti chips to get residual oxygen during the anneal. All samples were rapidly quenched in water after the desired annealing time was achieved, resulting in brief exposure to air while hot. This oxidized layer was ground off before further analysis or exposure. Microstructures resulting from annealing temperatures of 1200 and 1350 °C (for 100 h) were compared. To further investigate the stability range of the σ phase, an anneal at 1450 °C (for 20 h) was also included.

Microstructure and Phase Analysis: For microstructure and phase analysis of the AC and AN states, as well as after oxidation, samples were embedded in a graphite-filled phenolic mounting compound, using a hot press (25 kN, 180 °C, 7 min). Prior to embedding, the oxidized samples were coated with an Au layer (≈ 4 nm) by plasma vapor deposition and afterward Ni-plated using an electrochemical bath. The embedded samples were ground using P320, P500, P800, P1200, and P2400 grit SiC paper with water before final polishing with 3 μ m and 1 μ m diamond suspensions and a lubricant consisting of ethylene glycol, ethanol, and isopropyl alcohol.

XRD (Bruker D8 Advance) and the “ICDD” materials database were used to identify the phases and determine the lattice parameters (LPs) of the cubic (Cr,Mo)-solid solution and the intermetallic (Cr,Mo)₃Si phase. The XRD system was equipped with a Cu cathode as the X-ray source using a Ni filter to block the β -line of Cu. Absorption correction for thick samples was performed as described in ref. [38]. A z-scan was performed before every measurement to minimize the z-position error.

Electron microscopy (Hitachi FlexSEM 1000II) was used to generate back-scattered electron (BSE) images of the microstructures and wavelength-dispersive X-ray spectroscopy (WDS) was used to measure the overall and local phase compositions and generate semiquantitative elemental distribution maps. The BSE images and the software “ImageJ.S” were used to determine the fractions of the different phases. The phase compositions of all samples were determined using at least ten WDS measurements per phase. The overall composition was calculated by taking into account the observed area fraction of each phase as determined via “ImageJ.” In the case of a single-phase material, the overall composition was determined using a WDS grid measurement and averaging over 121 points.

High-Temperature Exposure and Thermogravimetry: To investigate and compare the oxidation and nitridation behavior of the alloys, annealed cuboids (ca. $4 \times 4 \times 3.5$ mm³), cut by electrical discharge machining and then ground using SiC paper up to P1200 grit, were exposed in a box furnace (Nabertherm HTC 03/15) in static laboratory air at 1200 °C. Prior to the exposure the cuboids were ultrasonically cleaned with acetone and isopropyl alcohol. The ramp from RT to 1200 °C was 10 K min⁻¹ and the samples were furnace cooled after 50 h.

To follow mass changes accurately, samples annealed at 1350 °C in Ar/5%H₂ for 100 h and then quenched were additionally measured in a TGA system in flowing (205 cm h⁻¹) dry synthetic air (80% N₂, 20% O₂) at 1200 °C (Furnace Nabertherm type HT 04/17). The mass change was continuously measured (Precision balance M25D-V, Sartorius) during the 100 h high-temperature exposure with one weight measurement per minute. The samples were connected to the balance via a vertical hanging sample holder system consisting of Pt wire and alumina tubes placed in the tube furnace. The linear Pt volatilization was taken into account by performing a reference measurement (empty sample holder) before loading the actual sample. The ramp rate was adjusted to prevent exceeding 1200 °C (RT to 1100 °C at 15 °C min⁻¹, 1100–1190 °C at 10 °C min⁻¹, and 1190–1200 °C at 5 °C min⁻¹). After 100 h exposure at 1200 °C, the furnace was shut down and the sample was furnace cooled under continuing gas flow. Reproducibility was confirmed by repeating most of the experiments.

Acknowledgements

The authors gratefully acknowledge the German Federal Ministry for Economic Affairs and Climate Action (BMWK) for the financial support of the project under grant no. 20E2125 based on a decision of the

German Bundestag. The authors thank Dr. G. Schmidt from DECHEMA-Forschungsinstitut (DFI) for the EPMA–WDS measurements and the members of the DFI workshop Heinrich Kopietz, Yvonne Hohmann, and Jano Bender for electrical discharge machining of the samples.

Open Access funding enabled and organized by Projekt DEAL.

Conflict of Interest

The authors declare no conflict of interest.

Data Availability Statement

The data that support the findings of this study are available from the corresponding author upon reasonable request.

Keywords

alloy development, chromium, high-temperature oxidation, molybdenum, refractory metal alloys

Received: November 13, 2023

Revised: March 14, 2024

Published online:

- [1] H. Harada, in *Congress, Proc. of the Inter. Gas Turbine IGTC2003Tokyo KS-2*, Tokyo **2003**.
- [2] J. H. Perepezko, *Science* **2009**, 326, 1068.
- [3] J. Wadsworth, T. G. Nieh, J. J. Stephens, *Int. Mater. Rev.* **1988**, 33, 131.
- [4] Y. F. Gu, H. Harada, Y. Ro, *J. Min. Met. Mater. Soc.* **2004**, 56, 28.
- [5] E. M. Savitskii, G. S. Burkhanov, *Physical Metallurgy of Refractory Metals and Alloys*, Consultants Bureau, New York **1970**, pp. 16–22; 193–199.
- [6] T. M. Pollock, S. Tin, *J. Propuls. Power* **2006**, 22, 361.
- [7] DERA, *Raw Material Price Monitor*, Federal Institute for Geosciences and Natural Resources **2023**, https://www.deutsche-rohstoffagentur.de/DERA/DE/Aktuelles/Monitore/2023/04-23/2023-04-preismonitor.pdf?sessionid=F658A5485A604D868B505C4BFCB7BA9B.internet961?__blob=publicationFile&v=2.
- [8] I. Murriss, Y. P. Jacob, V. A. C. Haanappel, M. F. Stroosnijder, *Oxid. Met.* **2001**, 55, 307.
- [9] S. Mathieu, *Oxid. Met.* **2010**, 74, 79.
- [10] A. Solimani-Dorcheh, M. C. Galetz, *J. Min. Met. Mater. Soc.* **2016**, 68, 2793.
- [11] H. Johanse, G. Asai, *J. Electrochem. Soc.* **1954**, 101, 604.
- [12] O. N. Carlson, L. L. Sherwood, F. A. Schmidt, *J. Less-Common Met.* **1964**, 6, 439.
- [13] K. Ioroi, Y. Aono, X. Xu, T. Omori, R. Kainuma, *J. Phase Equilib. Diffus.* **2022**, 43, 229.
- [14] A. Solimani-Dorcheh, M. C. Galetz, *Oxid. Met.* **2015**, 84, 73.
- [15] Y. Aono, T. Omori, R. Kainuma, *Intermetallics* **2019**, 112, 106526.
- [16] P. Pfizenmaier, A. S. Ulrich, U. Glatzel, M. C. Galetz, *Metals* **2021**, 11, 1072.
- [17] A. Solimani, T. Nguyen, J. Zhang, D. J. Young, M. Schütze, *Corros. Sci.* **2020**, 176, 109023.
- [18] S. V. Raj, *Mater. Sci. Eng. A* **1995**, 201, 229.
- [19] W. Trzebiatowski, H. Ploszek, J. Lobzowski, *Anal. Chem.* **1947**, 19, 93.
- [20] A. S. Ulrich, P. Pfizenmaier, A. Solimani, U. Glatzel, M. C. Galetz, *Corros. Sci.* **2020**, 165, 108376.

- [21] F. Hinrichs, A. Kauffmann, A. S. S. D. Tirunilai, B. Beichert, G. Winkens, K. U. A. S. Beck, M. C. Galetz, Z. Long, H. Thota, Y. Eggeler, A. Pundt, M. Heilmaier, *Corros. Sci.* **2022**, 207, 110566.
- [22] L. Pandelaers, R. Schmid-Fetzer, *Landolt-Börnstein: Ternary Alloy Systems, Subvolume E, Refractory Metal Systems*, Springer, Berlin **2010**, pp. 182–191.
- [23] H. Wu, C. Li, C. Guo, Z. Du, *J. Alloys Compd.* **2022**, 922, 166164.
- [24] H. Wu, C. Li, C. Guo, Z. Du, *Calphad* **2023**, 83, 102631.
- [25] E. Rudy, H. Nowotny, *Chem. Monthly* **1974**, 105, 156.
- [26] M. Venkatraman, J. P. Neumann, *Bull. Alloy Phase Diagrams* **1987**, 8, 216.
- [27] H. Nowotny, H. Schroth, R. Kieffer, F. Benesovsky, *Monatsh. Chem.* **1953**, 84, 579.
- [28] A. S. Ulrich, P. Pfizenmaier, A. Solemani, U. Glatzel, M. C. Galetz, *Int. J. Refract. Met. Hard Mater.* **2018**, 76, 72.
- [29] M. Guerin, F. Rakotovo, S. Y. Brou, G. Bonnet, B. Panicaud, J. L. Grosseau-Poussard, P. Goudeau, *J. Alloys Compd.* **2017**, 718, 223.
- [30] P. Kofstad, K. P. Lillerud, *J. Electrochem. Soc.* **1980**, 127, 2410.
- [31] E. A. F. T. Polman, P. J. Gelings, *Oxid. Met.* **1989**, 32, 433.
- [32] L. Latu-Romain, Y. Parsa, Y. Wouters, *Mater. Charact.* **2019**, 152, 58.
- [33] L. Latu-Romain, Y. Parsa, S. Mathieu, M. Vilasi, M. Ollivier, A. Galerie, Y. Wouters, *Oxid. Met.* **2016**, 86, 497.
- [34] A. S. Ulrich, U. Glatzel, M. C. Galetz, *Oxid. Met.* **2021**, 95, 445.
- [35] W. Hagel, *Trans. Am. Soc. Met.* **1963**, 56, 583.
- [36] C. A. Barrett, A. F. Presler, *Corest: A Fortran Computer Program to Analyze Paralineal Oxidation Behavior and Its Application to Chromic Oxide Forming Alloys*, National Aeronautics and space administration, Washington, D.C. **1976**.
- [37] J. L. Smialek, *High Temp. Corros. Mater.* **2023**, 99, 431.
- [38] J. B. Nelson, D. P. Riley, *Proc. Phys. Soc.* **1945**, 57, 160.
- [39] A. B. Gokhale, G. J. Abbaschian, *J. Phase Equilib.* **1991**, 12, 493.